

ACS SYMPOSIUM SERIES **770**

Imaging in Chemical Dynamics

Arthur G. Suits, EDITOR
Berkeley Laboratory

Robert E. Continetti, EDITOR
University of California



American Chemical Society, Washington, DC

Chapter 9

Ion Imaging in Surface Scattering

M. Maazouz¹, J. R. Morris^{1,2}, and D. C. Jacobs¹

¹Department of Chemistry and Biochemistry, University of Notre Dame,
Notre Dame, IN 46556

²Department of Chemistry, Virginia Polytechnic Institute and State
University, Blacksburg, VA 24061

Hyperthermal energy collisions between gas-phase molecular ions and solid surfaces are studied with a novel ion imaging detector that simultaneously records the mass, velocity, and scattering angle of product ions. Image processing techniques are employed to identify, in real time, individual ions appearing within each video frame. Representative ion/surface systems are presented to demonstrate how imaging techniques can be used to extract dynamical information about energy transfer, charge transfer, dissociation, and atom-abstraction processes.

Introduction

The reaction of hyperthermal energy ions with surfaces is important to a wide variety of applications, e.g., plasma processing in the microelectronics industry, space flight in low-earth orbit, and mass spectrometry. Hyperthermal ions with translational energies ranging from 10^0 - 10^3 eV can access reaction pathways that are closed to reagents under thermal conditions. Fundamental processes commonly occurring during ion/surface scattering are energy transfer, electron transfer, dissociative scattering, atom abstraction, sputtering, and ion implantation. In an effort to characterize the detailed dynamics associated with these processes, experiments are performed to probe the atomic motion of the ions as they approach, interact, and scatter from the surface. Novel instrumental techniques are required to detect the scattered products (electrons, neutrals, and ions of various masses) and to resolve their angular and velocity distributions. Scattering data along with theoretical simulations can provide a vivid picture of the complex mechanisms associated with hyperthermal energy gas/surface reactions.

A number of research groups have developed and applied ion detectors with energy-, mass-, and/or angular-resolution in an effort to carefully study ion/surface scattering. Heiland and coworkers measure the time-of-flight distributions of scattered atomic and molecular ions impinging on single-crystal surfaces at keV energies.⁽¹⁾ The Kleyn group has utilized an electrostatic sector in conjunction with time-of-flight methods to study the angle-resolved kinetic energy distributions

resulting when alkali ions and small molecular ions are scattered from surfaces.(2,3,4) Akazawa and Murata have utilized a rotatable mass-spectrometer to determine the angular distributions of products in the scattering of N_2^+ , CO^+ and CO_2^+ from a Pt(100) surface.(5,6) Cooks and coworkers employed a rotatable hybrid, tandem mass spectrometer of the BEEQ configuration (B, magnet analyzer; E, electrostatic analyzer (ESA); Q, quadrupole mass filter) to study reactions of polyatomic molecules with organic surfaces.(7) Winograd combined laser ionization methods with ion-imaging techniques to study the desorption of neutral particles under ion bombardment.(8)

Although these pioneering experiments successfully adapted many techniques that were originally developed within the gas-phase dynamics community, the complexity of gas/surface interactions limited researchers from obtaining the detailed dynamics that were routinely achieved in gas-gas scattering experiments. Furthermore, investigations into ion-surface reactions below 100 eV are scarce because of technical difficulties in preparing intense, collimated ion beams. In an attempt to bridge this gap, we have developed an ion/surface scattering apparatus that combines resonance-enhanced multiphoton ionization (REMPI), to prepare an incident beam of state-selected ions, with an ion imaging detector for collecting scattered ions.(9)

Ion imaging in gas-phase photodissociation was first employed by Chandler and co-workers to collect two-dimensional images of state-selected photofragments.(10,11) In the surface science community, ion imaging has been used to measure the angular and/or velocity distribution of ions desorbed under electron/photon impact.(12,13) Rabalais developed scattering and recoiling imaging spectroscopy (SARIS) as an analytical tool to accurately assign the structure of adsorbates on surfaces.(14) Ion imaging is complementary to time-of-flight methods in that the former records a spatial distribution at one point in time, while the latter records the temporal distribution at one point in space. However, ion imaging detectors generally have a larger solid angle of collection, and they simultaneously record velocity distributions for a wide series of scattering angles.

This chapter introduces a unique two-dimensional velocity, ion-imaging detector specifically designed for surface scattering experiments. In these experiments, one measures the fraction of incident ions which emerge from the surface having a particular mass, velocity, and scattering angle. Image processing algorithms are applied to the data in real-time to identify individual ions within each video frame. Results from various ion/surface systems are presented here to illustrate the capabilities of the ion-imaging detector and to show the type of dynamical information which can be obtained from its use.

Experimental Design

Scattering is performed in an ultrahigh vacuum chamber equipped with a source of state-selected ions, ion transport optics, a sample manipulator, an ion imaging detector, and standard surface science tools.(9) The ion source consists of a differentially-pumped molecular beam crossed by focused pulsed laser. A 20-Hz frequency-doubled, Nd:YAG-pumped dye laser provides 6-ns, tunable ultraviolet

light pulses for REMPI. The resulting packets of state-selected ions are accelerated by electrostatic optics, mass filtered, and decelerated before striking the surface.

Both incident and scattered ions are monitored using an ion imaging detector (flyswatter) with near single-ion collection efficiency.⁽¹⁵⁾ Figure 1 illustrates the configuration of the flyswatter relative to the final ion transport optics and the surface. The detector's ion optics have been improved since publication of the original design in Ref. 14. Figure 2a provides a cross-sectional view detailing the current arrangement of elements in the flyswatter detector. The flyswatter consists of a normally grounded repeller plate that runs parallel to a permanently grounded grid. The incident ions pass between the repeller and the grid before surface impact, and product ions traverse through this region after scattering from the surface. At a predetermined 'swat delay' relative to the laser trigger, a ~ 1000 V pulse, of equal polarity as the ions to be detected, is placed on the repeller plate, and a ~ 1000 V pulse, of opposite polarity, is placed on the flight tube. This action accelerates the ions in a direction normal to the plates while preserving their spatial distribution. After two stages of acceleration, the ions drift through a field-free flight tube before being accelerated into a pair of channel electron multiplier array (CEMA) plates. The 40-mm diameter, image-quality CEMA plates (Galileo) transform an incident ion into $\sim 10^7$ electrons. These secondary electrons accelerate toward a phosphor screen (Kimball Physics), biased +4 kV relative to the rear CEMA plate. The resulting burst of light (< 300 μm diameter) is captured by a charged coupled device (CCD) camera. The images are sent to a frame grabber board located inside a Macintosh G3 computer, where they are digitized, processed, and stored for analysis.

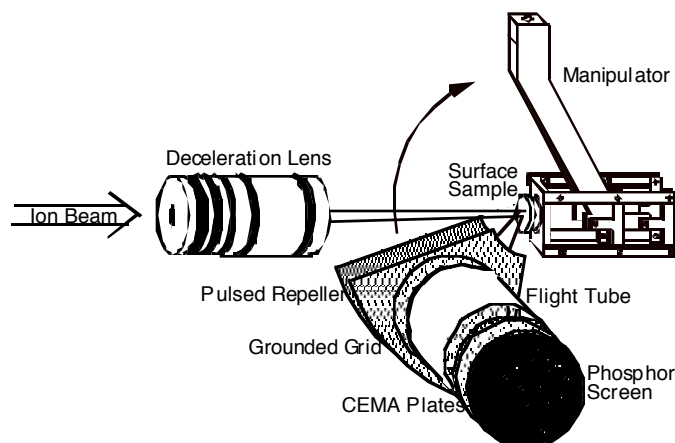


Figure 1. A schematic of the ion imaging detector (flyswatter). The ion beam exits the Menzinger deceleration lens and is directed toward the surface sample manipulator. Rotation of the detector about the surface increases the range of in-plane acceptance angles to $\pm 55^\circ$. (Reproduced with permission from reference 15. Copyright 1992 American Institute of Physics)

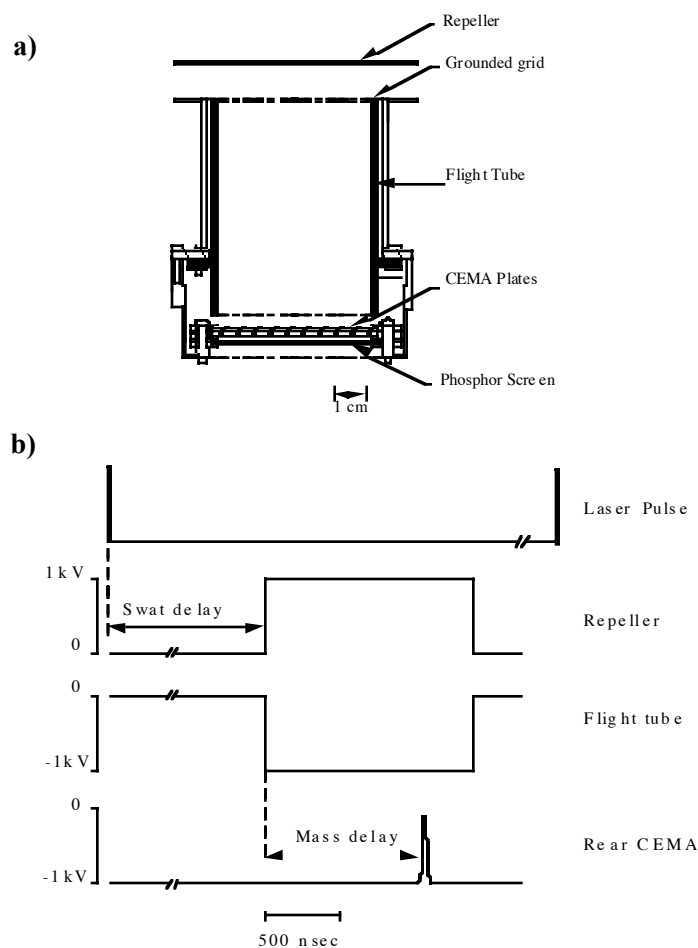


Figure 2. a) An assembly drawing of the flyswatter detector. b) Sequence of voltage pulses applied to the flyswatter optics.

Ions of different mass will experience different flight times through the detector. Lighter ions will have a larger velocity than heavier ions upon acceleration into the flight tube; hence, lighter ions will arrive at the CEMA plates earlier in time. The flyswatter exploits this idea to achieve mass-resolution. Wiley and McLaren developed a set of focusing conditions to compensate for the distribution of initial ion positions between the repeller and the grid when the swat pulse fires.⁽¹⁶⁾ More advanced optimizations can reduce the broadening associated with the dispersion of initial ion velocities along the direction normal to the repeller.⁽¹⁷⁾ By gating the CEMA plates, ions of only one particular mass are allowed to contribute to the resulting image. The pair of CEMA plates are simmered at 1100 VDC. At a preset

‘mass delay’ relative to the ‘swat pulse’ on the repeller, an additional 900 V pulse (Directed Energy, Inc.) of 25 ns duration is applied to the rear CEMA plate. During the ‘mass pulse’, the CEMA plates are biased with a total of 2000 V, and virtually every ion which impacts the CEMA plates produces a spatially localized electron cascade event. In contrast, ions that strike the CEMA plates before or after the mass pulse are amplified with negligible gain, because the CEMA plates have only a 1100 V bias. Consequently, images recorded by the slow, 30-Hz CCD camera represent the spatial distribution of mass-filtered ions recorded at a precise swat delay relative to the initial laser pulse. Figure 2b illustrates the overall pulse sequence applied to the flyswatter optics. Once the flight time, t_1 , corresponding to detection of ions having mass, m_1 , is known, any peak, t_2 , in the time-of-flight spectrum can be accurately assigned to an absolute mass, m_2 , by the relation:(9)

$$m_2 = m_1 \left(\frac{t_2}{t_1} \right)^2 \quad (1)$$

Geometrical constraints must also be considered in the overall analysis. The solid angle of collection for the imaging detector is defined by acceptance angles of $\pm 28^\circ$ (in-plane) and $\pm 7^\circ$ (out-of-plane). This corresponds to a collection efficiency of approximately 3.6% of 2π steradians. The detector is mounted on an 8" O.D. rotatable platform (Thermionics). In the most common configuration, both the incident ion beam and the detector lie along the surface normal. Rotation of the detector about the surface extends the range of in-plane acceptance angles to $\pm 55^\circ$. In addition, an azimuthal rotation of the surface sample allows for product ion collection within any crystallographic scattering plane.

The critical parameters in operating the flyswatter are the voltage pulse polarities, and the swat and mass delays. The incident ion packet can be detected if the repeller is fired shortly after the ions exit the Menzinger lens and before they leave the detection region. An image of the incident ion packet provides information regarding the spatial integrity of the ion beam as well as a quantitative measure of the number of incident ions. Figure 3 shows three ion images, recorded at successive swat delays, of the incident ion packet as it approaches the surface. For later swat delays, the incident ions have already impacted the surface, and scattered product ions can be detected. Positive and negative scattered ions are distinguished by the polarity of the voltages applied to the repeller pulse, the flight-tube pulse, and the CEMA front plate. Figure 4 shows an image of scattered positive ions recorded at a swat delay of 30 μ s. The entire velocity distribution of scattered products is measured by collecting mass-filtered images at a few different swat delays beginning with the time that scattered ions first reach the detector through the time that the slowest ions reach the detection region. Reducing ion images, recorded at various swat delays, to a velocity distribution is described in the “Velocity Analysis” Section below. At periodic intervals during scattering experiments, the swat and mass delays are set to record an image of the incident ion packet. The integrated intensity of the ion packet image is directly proportional to the number of ions incident on the surface, and this quantity is used to normalize the scattered product distributions. The relative ion yield of a given scattered product is calculated as the number of collected product ions, integrated over all velocities within the angular range of the detector, divided by the number of incident ions.

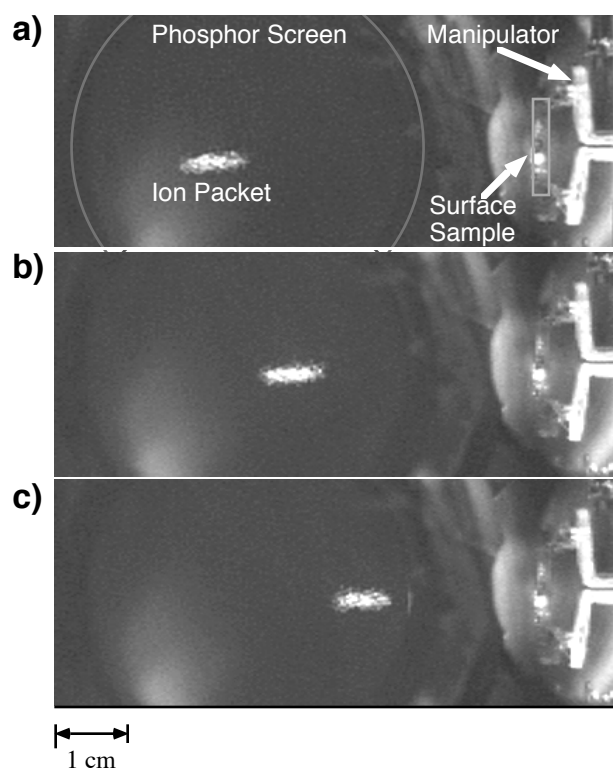


Figure 3. Image of incident NO^+ ions approaching the surface. The manipulator, surface sample, and phosphor screen are marked. Swat delays are (a) $20.0 \mu\text{s}$, (b) $21.0 \mu\text{s}$, and (c) $22.0 \mu\text{s}$.

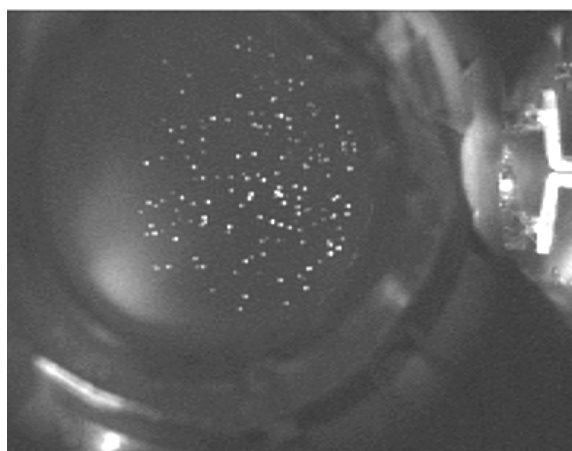


Figure 4. Image of scattered NO^+ ions at a swat delay of $30 \mu\text{s}$.

Image Analysis

The images appearing on the phosphor screen are viewed through a standard vacuum window, 25 cm away. A CCD camera (NEC TI-324A) records the image, and a frame grabber board (National Instruments PCI-1408), resident in a Macintosh G3 computer, digitizes the image for analysis. Frame integration on the water-cooled CCD chip is an efficient method to reduce the average amount of dark counts, readout noise, and bit noise associated with frame-grabber digitization. A computer-interfaced timing circuit synchronizes image capturing to the 20-Hz pulsed-laser system. The timing circuit initiates frame integration on the CCD chip and provides an external trigger pulse for the frame grabber board when the CCD camera is ready to transmit its image after a selected number of laser shots (typically 5 - 40). The frame grabber digitizes an entire video frame in 1/30 s and the process of frame-integration on the CCD chip is repeated while the computer processes the last acquired image.

The image analysis software is written in National Instruments' graphical-programming language, LabVIEW-IMAQ. The frame-grabber board passes an 8-bit raw image to the LabVIEW acquisition program. The software converts the 8-bit image to a 16-bit image, subtracts a background image recorded previously, and filters the difference image before thresholding. The table below shows the 9 x 9 Kernel filter that is applied to the image.

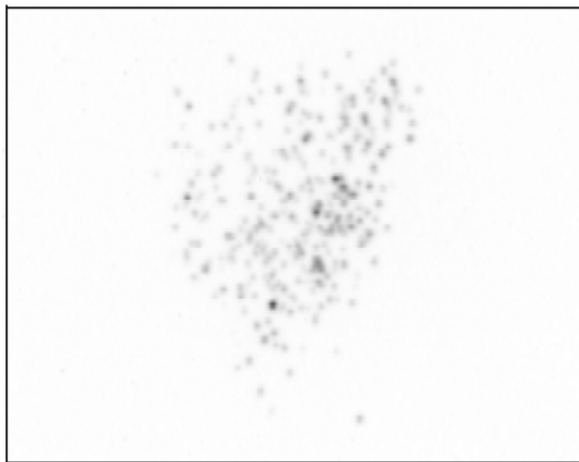
Table I. Kernel for filtering Particles

0	0	0	-1	-1	-1	0	0	0
0	-1	-1	-3	-3	-3	-1	-1	0
0	-1	-3	-3	-1	-3	-3	-1	0
-1	-3	-3	8	12	8	-3	-3	-1
-1	-3	-1	12	20	12	-1	-3	-1
-1	-3	-3	8	12	8	-3	-3	-1
0	-1	-3	-3	-1	-3	-3	-1	0
0	-1	-1	-3	-3	-3	-1	-1	0
0	0	0	-1	-1	-1	0	0	0

The filter has the effect of amplifying the signal from ions, which illuminate 5 - 9 contiguous pixels, and reducing the intensity of individual hot pixels, which represent background noise. Figure 5a shows an image after background subtraction, and Fig. 5b shows the same image after the Kernel filter has been applied. The filter clearly distinguishes individual ions that are more than 600 μm apart. Ions of different intensity in Fig. 5a appear more equitable in Fig. 5b. The acquisition software then converts the 16-bit filtered image back to an 8-bit image to expedite further

processing. A particle-detection routine is applied to the filtered image to identify individual ions. The criterion for an ion is that four or more contiguous pixels must have an intensity greater than a selected threshold value. The x and y coordinates of all particles meeting the above criterion are recorded in a text file. Digitizing and processing a single video frame (640 x 480 pixels) requires 1.3 s of CPU time. During this processing time, the CCD camera is acquiring the next image via frame-integration on the CCD chip. In a typical experimental run, a few hundred video frames, each representing the scattering of 40 ion packets (laser shots), are digitized and processed.

a)



b)

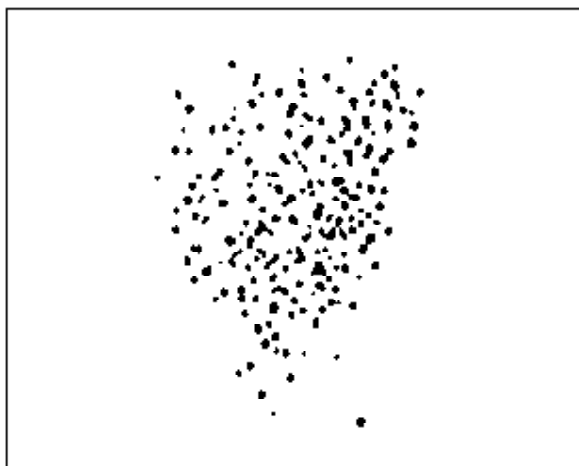


Figure 5. (a) Image of scattered ions after background subtraction. (b) Same image after filtering and thresholding.

Velocity Analysis

To compile a complete velocity distribution of a scattered product, ion images must be gathered at a few different swat delays. This is because scattered ions routinely have broad velocity distributions that extend beyond the dimensions of the image detector for any single swat delay. Real-time processing of the images results in a list of (x, y) coordinates for each detected ion. The list of ion events is transformed into a velocity distribution by a separate velocity analysis program. Characterization of the incident ion packet allows one to determine the (x, y) position and the time at which the incident ion packet strikes the surface. Relative to this reference point, the velocity of all scattered ions can be determined from the distance traveled between the point of surface impact and the scattered ion position, divided by the time lapsed between surface impact and scattered-ion collection (swat delay + mass delay). Appropriate weightings for each ion are calculated from geometrical considerations.⁽¹⁵⁾ A 2-D velocity distribution is generated by sorting the recorded ion events into a 2-D velocity grid and assigning the relative intensity in each grid element to the sum of the relevant ion weightings. This can be collapsed to a 1-D velocity distribution by integrating the 2-D velocity distribution over all final scattering angles.

Results

A variety of ion/surface scattering systems have been studied with the flyswatter detector. Representative systems are briefly presented below to demonstrate how the flyswatter can provide unique data for deciphering the dynamics of complex reaction mechanisms.

Dissociative scattering at surfaces can occur through a number of mechanisms.⁽¹⁸⁾ In the scattering of $\text{OCS}^+(\text{X } ^2\Pi)$ on $\text{Ag}(111)$, three different anionic fragments are observed. Figure 6 shows the time-of-flight mass spectrum resulting from $\text{OCS}^+(\text{X } ^2\Pi)$ colliding with $\text{Ag}(111)$ at 65 eV and normal incidence.⁽¹⁹⁾ Equation 1 converts the peaks in the time-of-flight distribution to exact masses. The fragment velocity distributions measured by the flyswatter detector, in conjunction with the dependence of the fragment yields on collision energy, provided evidence for assigning the O^- , S^- , and SO^- product channels to three distinct fragmentation mechanisms: prompt impulsive dissociation, dissociative neutralization, and atom elimination.

Atom abstraction is an elementary process by which an atom is transferred to or from an incident molecule as the molecule impacts a surface. Hyperthermal energy $\text{NO}^+(\text{X } ^1\Sigma^+)$ ions were found to abstract oxygen from $\text{O}/\text{Al}(111)$ to produce scattered NO_2^- ions.⁽²⁰⁾ Figure 7 shows the velocity distribution of NO_2^- products formed from $\text{NO}^+(\text{X } ^1\Sigma^+)$ incident on $\text{O}/\text{Al}(111)$ at 40 eV. The velocity distribution of scattered NO_2^- products is nonthermal and cannot be described by a Maxwell-Boltzmann distribution at the surface temperature. Moreover, the mean translational energy of scattered NO_2^- increases with NO^+ collision energy. These results implicate a direct, Eley-Rideal reaction mechanism, whereby an incident molecule collides with an adsorbed O-atom and reacts without ever becoming thermally accommodated with the surface.

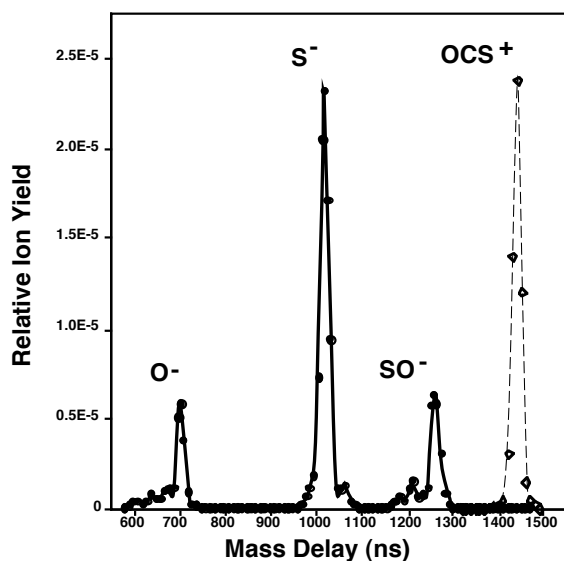


Figure 6. Time-of-flight mass-spectrum of incident OCS^+ ions (\diamond) and scattered negative ions (\bullet) formed through collisions between 65 eV OCS^+ and a $\text{Ag}(111)$ surface. From left to right, the atomic masses of the four major peaks are 16, 32, 48, and 60 amu. (Reproduced with permission from reference 20. Copyright 1997 American Institute of Physics)

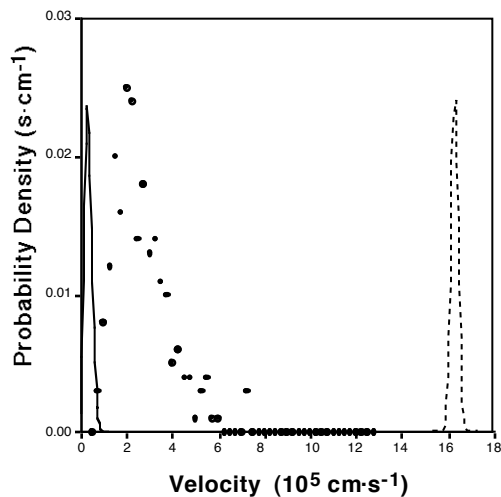


Figure 7. Velocity distribution for NO_2^- (\bullet) formed from NO^+ abstracting an oxygen atom from $\text{O}/\text{Al}(111)$. For comparison, the plot shows the velocity distribution (dashed line) of incident NO^+ , and the predicted Maxwell-Boltzmann distribution (solid line) if NO_2^- were thermally equilibrated with the surface at 298 K.

The scattering of state-selected $\text{NO}^+(\text{X } ^1\Sigma^+, v=0-6)$ on $\text{GaAs}(110)$ exhibits a variety of fundamental processes: energy transfer, charge transfer, and fragmentation. A dynamical study of O^- product formation was undertaken to explore the interplay between electron transfer and impulsive dissociation events. Vibrational energy in incident NO^+ was found to be ten times more effective than collision energy in enhancing the O^- yield.(9) Model calculations suggest that electron transfer immediately prior to surface impact creates a quantum mechanical vibrational coherence in the molecule.(21) Figure 8 shows the probability density for the O^- product as a function of its final velocity and scattering angle.(22) Images were collected for a number of detector orientations to increase the range of acceptance angles. Although NO^+ was incident along the surface normal, the scattering distribution in Fig. 8 reveals a striking angular asymmetry, not unlike the asymmetric structure of $\text{GaAs}(110)$, shown in the inset of Fig. 8. Trajectory simulations along with an empirical opacity function are able to reproduce the scattering data. The opacity function relates the probability for electron attachment to the oxygen fragment's final surface impact parameter. The probability is found to peak along the lattice rows where dangling bond states reside.

Ion imaging techniques have provided valuable data for understanding the many reaction pathways available to hyperthermal energy, gas/surface collisions. The National Science Foundation (CHE96-15878) is gratefully acknowledged for their support of this work.

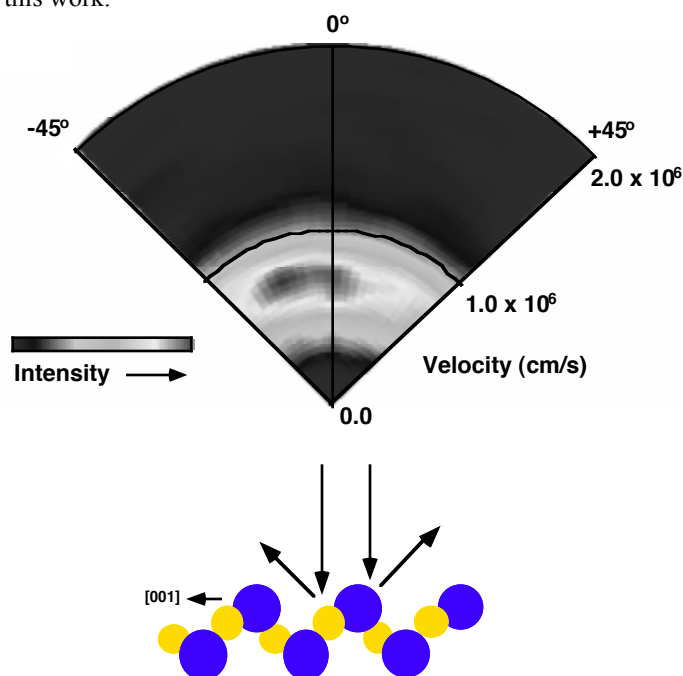


Figure 8. Probability density for scattered $\text{O}^- (^2P)$ fragments as a function of final velocity and scattering angle. $\text{NO}^+(\text{X } ^1\Sigma^+, v=1)$ is incident along the surface normal of $\text{GaAs}(110)$ with 45 eV collision energy. The scattering plane lies along the $[001]$ symmetry direction of $\text{GaAs}(110)$.

References

1. Heiland, W in *Low Energy Ion-Surface Interactions*; Rabalais, J.W.; Ed.; Wiley Series in Ion Chemistry and Physics; Wiley & Sons Inc.: New York, NY, 1994, p. 313-354
2. Reijnen, P.H.F.; Kleyn, A.W. *J. Chem. Phys.* **1989**, *139*, 489-496
3. Horn, T.M.; Haochang, P.; van den Hoek, P.J.; Kleyn, A.W. *Surf. Sci.* **1988**, *201*, 573-602
4. Tenner, A.D.; Gillen, K.T.; Horn, T.M.; Los, J.; Kleyn, A.W. *Surf. Sci.* **1986**, *172*, 90-120
5. Akazawa, H.; Murata, Y. *J. Chem. Phys.* **1990**, *92*, 5560-5568
6. Akazawa, H.; Murata, Y. *Surf. Sci.* **1989**, *207*, L971-L979
7. Miller, S.A.; Luo, H.; Jiang, X.; Rohrs, H.W.; Cooks, R.G. *Int. J. Mass Spec. Ion Proc.* **1997**, *160*, 83-105
8. Kobrin, P. H.; Schick, G. A.; Baxter, J. P.; Winograd, N. *Rev. Sci. Instrum.* **1986**, *57*, 1354-1362
9. Martin, J.S.; Greeley, J.N.; Morris, J.R.; Feranchak, B.T.; Jacobs, D.C.; *J. Chem. Phys.* **1994**, *100*, 6791-6812
10. Chandler, D.W.; Houston, P.L. *J. Chem. Phys.* **1987**, *87*, 1445-1447
11. Thoman, J. W.; Chandler, D.W.; Parker, D.H.; Janssen, M.H.M. *Laser Chem.* **1988**, *9*, 27-46
12. Dresser, M.J.; Alvey, M.D.; Yates, J.T. Jr. *J. Vac. Sci. Technol. A* **1986**, *4*, 1446-1450
13. M. Menges et al., Springer Ser. Surf. Sci. 31, 275, Berlin, Springer-Verlag (1992)
14. Kim, C.; Höfner, C.; Rabalais, J. W. *Surf. Sci.* **1997**, *388*, L1085-L1091
15. Corr, D.; Jacobs, D. C. *Rev. Sci. Instrum.* **1992**, *63*, 1969-1972
16. Wiley, M.C.; McLaren, I.H. *Rev. Sci. Instrum.* **1955**, *26*, 1150
17. Chandezon, F.; Huber, B.; Ristori, C. *Rev. Sci. Instrum.* **1994**, *65*, 3344-3353
18. Morris, J. R.; Kim, G.; Barstis, T. L. O.; Mitra, R.; Quinteros, C. L.; Jacobs, D. C. *Nuc. Instrum. Meth. B* **1997**, *125*, 185-193
19. Morris, J. R.; Kim, G.; Barstis, T. L. O.; Mitra, R.; Jacobs, D. C. *J. Chem. Phys.* **1997**, *107*, 6448-6459
20. Maazouz, M.; Barstis, T. L. O.; Maazouz, P.; Jacobs, D. C. *Phys. Rev. Lett.* **2000**, *84*, 1331-1334
21. Qian, J. ; Jacobs, D. C.; Tannor, D. J. *J. Chem. Phys.* **1995**, *103*, 10764-10778
22. Morris, J. R.; Martin, J. S.; Greeley, J. N.; Jacobs, D. C. *Surf. Sci.* **1995**, *330*, 323-336